

Aluminum textile-based binder-free nanostructured battery cathodes using a layer-by-layer assembly of metal/metal oxide nanoparticles


F SCI


Cite as: Appl. Phys. Rev. **8**, 011405 (2021); <https://doi.org/10.1063/5.0039990>

Submitted: 09 December 2020 . Accepted: 26 January 2021 . Published Online: 18 February 2021

 Donghyeon Nam,  Minseong Kwon, Yongmin Ko, June Huh,  Seung Woo Lee, and  Jinhan Cho

COLLECTIONS

 This paper was selected as Featured

 This paper was selected as Scilight



View Online



Export Citation



CrossMark

ARTICLES YOU MAY BE INTERESTED IN

[Textile-based cathodes for lithium-ion batteries](#)

Scilight **2021**, 081102 (2021); <https://doi.org/10.1063/10.0003597>

[Cellular automata dynamics of nonlinear optical processes in a phase-change material](#)

Applied Physics Reviews **8**, 011404 (2021); <https://doi.org/10.1063/5.0015363>

[Quantitative digital microscopy with deep learning](#)

Applied Physics Reviews **8**, 011310 (2021); <https://doi.org/10.1063/5.0034891>



Applied Physics Reviews

Impact matters.

17.054

JOURNAL IMPACT FACTOR

Aluminum textile-based binder-free nanostructured battery cathodes using a layer-by-layer assembly of metal/metal oxide nanoparticles



Cite as: Appl. Phys. Rev. **8**, 011405 (2021); doi: 10.1063/5.0039990

Submitted: 9 December 2020 · Accepted: 26 January 2021 ·

Published Online: 18 February 2021



View Online



Export Citation



CrossMark

Donghyeon Nam,¹ Minseong Kwon,¹ Yongmin Ko,² June Huh,¹ Seung Woo Lee,^{3,a)} and Jinhan Cho^{1,a)}

AFFILIATIONS

¹Department of Chemical and Biological Engineering, Korea University, 145 Anam-ro, Seongbuk-gu, Seoul 02841, Republic of Korea

²Division of Energy Technology, Materials Research Institute, Daegu Gyeongbuk Institute of Science and Technology (DGIST), 333 Techno Jungang-daero, Hyeonpung-eup, Dalseong-gun, Daegu, 42988, Republic of Korea

³The George W. Woodruff School of Mechanical Engineering, Georgia Institute of Technology, Atlanta, Georgia 30332, USA

^{a)}Authors to whom correspondence should be addressed: seung.lee@me.gatech.edu and jinhan71@korea.ac.kr

ABSTRACT

Despite considerable interest in textile-based battery electrodes with large surface areas and mechanical flexibility, issues have restricted further advances in the energy performance of textile electrodes. These issues include the ineffective incorporation of conductive and/or active components into textile frameworks, the poor charge transfer between energy materials, and the formation of numerous unstable interfaces within textile electrodes. Herein, we introduce an aluminum textile-based lithium-ion battery cathode with remarkable areal capacity, high rate performance, and good cycling stability. Ligand exchange reaction-induced layer-by-layer (LbL) assembly of metal nanoparticles and small molecule linkers, with subsequent metal electroplating, perfectly converted polyester textiles to 3D-porous aluminum textiles that can be used as current collectors and high-energy reservoirs. The consecutive LbL assembly of high-energy LiFePO₄ and conductive indium tin oxide nanoparticles onto the aluminum textiles using small organic linkers significantly increased the areal capacity and cycling stability (at least 580 cycles) of the resultant cathode, allowing facile charge transfer within the textile electrodes. Furthermore, the areal capacity of these textile electrodes increased from 1.07 to 3.28 mA h cm⁻², with an increase in the folding number from 0 to 2.

Published under license by AIP Publishing. <https://doi.org/10.1063/5.0039990>

I. INTRODUCTION

The explosive growth of and interest in portable and wearable electronic systems has fostered the development of lithium-ion batteries (LIBs) with higher energy and power densities and longer lifetimes.¹⁻⁵ In particular, substantial research has focused on improving the energy density of LIBs by employing high-voltage cathodes, high-capacity silicon anodes, or lithium-metal anodes.⁶⁻⁸ In contrast, relatively little effort has been devoted to the design of electrodes with high surface areas, although areal performance indexes, including the areal capacity, areal energy density, and areal power density, are particularly important for the practical use of energy storage devices. Theoretically, the areal energy density of LIBs can be improved by increasing the thickness or loading amount of active electrode materials per unit area. However, the electrode thickness is limited due to the performance loss (especially power density) associated with significant internal charge transport resistances, thus, making the achievement of both high areal energy and power densities difficult.⁹⁻¹¹ Additionally, when

LIB electrodes with active materials thickly coated on conventional metal foil current collectors undergo bending or folding motions, the active materials tend to delaminate from the current collector due to the residual stress generated between the active materials and metal foils.^{12,13} Therefore, to resolve these drawbacks, current collectors with stress-relieving properties and a high mass loading of active materials should be preferentially developed. Additionally, favorable interfacial interactions and facile charge transfer are necessary between the current collector and active materials as well as between adjacent active materials for both stability and high power densities.^{14,15} If LIB electrodes can meet these requirements, they can exhibit improved areal performances, and simultaneously overcome the troublesome performance dilemma between areal energy and power densities.

A promising strategy for achieving both high energy and power densities is to employ binder-free nanostructured electrodes with conductive porous metal substrates such as metal foam to enable rapid electron and ion transport to active electrode materials.¹⁶⁻¹⁸ Although

conventional polymer-binder-incorporated slurries can significantly increase the mass loading amount of active materials within electrodes, they have an adverse effect on the charge-transfer kinetics and can be restrictedly applied to only flat and nonporous substrates rather than to 3D porous substrates. In addition, the use of poly(vinylidene fluoride) (PVDF) limits the sufficient accommodation of the volume expansion of conventional active materials due to its poor interfacial interactions, thus leading to poor cycling stability.

Flexible and porous textiles have emerged as promising alternative current collectors for multifunctional energy storage devices, including supercapacitors and LIBs because of their superior mechanical properties, stress-relieving properties, and high surface areas.^{12,19–24} For this approach, the insulating textile substrate must be coated with conductive and active materials. For example, electrically conductive components [e.g., carbon nanotubes (CNTs), reduced graphene oxides, and metal nanowires] and large-sized (more than a few micrometers) active materials have been introduced into 3D porous textiles through physical adsorption processes (e.g., dip coating, painting, printing, or doctor blading)^{25–28} and electroless deposition (chemical reduction) of metal ions.^{3,23,29} However, in most cases, these approaches, which lack specific consideration of interfacial interactions, have poor control over the loading amount and the coating quality of conductive materials and active materials, limiting the full utilization of the surface area of porous textiles. However, despite the use of porous metal substrates, most studies using binder-free electrodes (including nonporous foil-based and 3D porous textile-based electrodes) are still based on small mass loading of active electrode materials ($<10\text{ mg cm}^{-2}$). Additionally, the interfacial interactions between neighboring active materials as well as between active materials and the current collector have not been deeply considered, resulting in poor mechanical flexibility of binder-free electrodes. Furthermore, to our knowledge, the maximum loading amount of active materials for binder-free LIB cathodes was estimated to be 8 mg cm^{-2} (areal capacity $\sim 1.3\text{ mA h cm}^{-2}$), and most cathodes exhibited even lower areal capacities, below $\sim 1\text{ mA h cm}^{-2}$.^{17,19,20,30–34}

Although additional metal electrodeposition can be conducted after the chemical reduction of metal ions, this approach cannot resolve the nonuniform metal coating originating from electroless deposition. Moreover, given that the metals used for electroplating are mainly Ni and Cu, which have low corrosion stability at high operating voltages ($>3.5\text{ V}$), the previously reported electrodeposited metal layers are more suitable for the current collectors of LIB anodes than for cathodes.^{35–38} Aluminum (Al) is highly advantageous for cathode current collectors requiring high operation voltages, but electroplated Al textile-based cathodes have never been reported to date, presumably due to the much lower reduction potential of Al (-1.66 V) than of water-splitting (-0.83 V) in aqueous solution. Therefore, the development of a 3D, porous Al current collector with a high surface area and excellent mechanical stability would be a breakthrough in textile-based LIB research.

Layer-by-layer (LbL) assembly is one of the most versatile solution processes for preparing organic/inorganic nanocomposite films with desired functionalities through complementary interactions between adjacent components irrespective of the substrate size and shape.^{39–44} Motivated by these advantages, a small number of research groups reported that electrostatic LbL-assembled CNTs, graphene oxides, and/or conducting polymers in water could be used as thin film components for LIB cathodes without polymer binders.⁴⁵ However, these electrostatically LbL-assembled organic electrodes

limit the type of available active materials, which also have poor areal capacity due to the low amount of adsorbed active materials.⁴⁶

Here, we introduce Al textile-based binder-free LIB cathodes with high mass loadings of active materials (up to $\sim 32\text{ mg cm}^{-2}$), large areal capacities (up to 3.28 mA h cm^{-2}), fast rate capabilities, and high operation stability (max ~ 580 cycles) (Fig. 1). Particularly, the main goal of our study is the preparation of an Al textile-based current collector with a large surface area and metal-like electrical conductivity by combining the respective advantages of ligand exchange LbL assembly using covalent bonding in organic media and metal electrodeposition. Additionally, we highlight that the mass loading of active materials and the areal capacity of the textile electrode are further scalable by increasing the bilayer number in our LbL assembly approach. To this end, a highly uniform and conductive Al textile as a 3D porous cathode current collector was first prepared through metal nanoparticle (NP) assembly-induced Al electroplating onto cotton textiles. The newly fabricated Al-electroplated textiles (Al-ET) in our study are prepared by coating the cotton fibrils with conductive LbL-assembled metal NP seeds (TOA-Au NPs, TOA-Cu NPs, or TOA-Ag NPs), then electroplating with Ni, and finally further metalized by Al electroplating in an ionic liquid. In this case, the formed Al-ET exhibits high conductivity (sheet resistance $\sim 0.02\ \Omega\ \text{sq}^{-1}$) with flexible mechanical properties (maintaining 82% of the initial conductivity after a 3000-cycle crumpling test and two-folding).

After Al electroplating onto cotton textiles (i.e., after the preparation of Al textile-based current collector), 35 nm-sized LiFePO_4 nanoparticles (LFP NPs) with high dispersion stability in toluene were sequentially LbL-assembled with 8 nm-sized indium tin oxide NPs (ITO NPs) in toluene with the aid of amine (NH_2)-functionalized small molecule linkers ($M_w \sim 103\text{ g mol}^{-1}$). Notably, this ligand exchange LbL assembly can generate metal oxide films and electrodes with a mechanically robust structure due to the high affinity between the LFP and ITO NPs and NH_2 groups of the molecular linkers as well as between the Al-ET current collector and the LFP and ITO NPs. This alternating deposition of active LFP NPs and conductive ITO NPs can facilitate charge transfer through the electrodes and allows efficient utilization of the redox reaction of LFP NPs, resulting in significant improvements in the areal capacity, specific capacity, and rate capability. Furthermore, the highly flexible nature of the Al-ETs and the robust mechanical properties of the NP-assembled Al-ETs enable consecutive multiple folding of the textile electrodes, achieving an unprecedented high areal capacity of $\sim 3.28\text{ mA h cm}^{-2}$. We also demonstrate that OA- Fe_3O_4 NPs can be LbL-assembled onto Ni-electroplated textiles for LIB anodes, which can then be easily combined with the prepared cathodes to yield full-cell LIBs. This work highlights the central role of the LbL-assembly-induced Al electroplating approach and the additional assembly process of high-energy and conductive NPs through ligand exchange reactions in manufacturing high-performance and flexible textile electrodes and provides a flexibility-based approach for designing and exploiting electrodes for various electrochemical devices.

II. RESULTS AND DISCUSSION

A. Conductive seed layer using LbL-assembled metal NPs

For this study, tetraoctylammonium bromide (TOA)-stabilized Au NPs (TOA-Au NPs) were LbL-assembled with diethylenetriamine

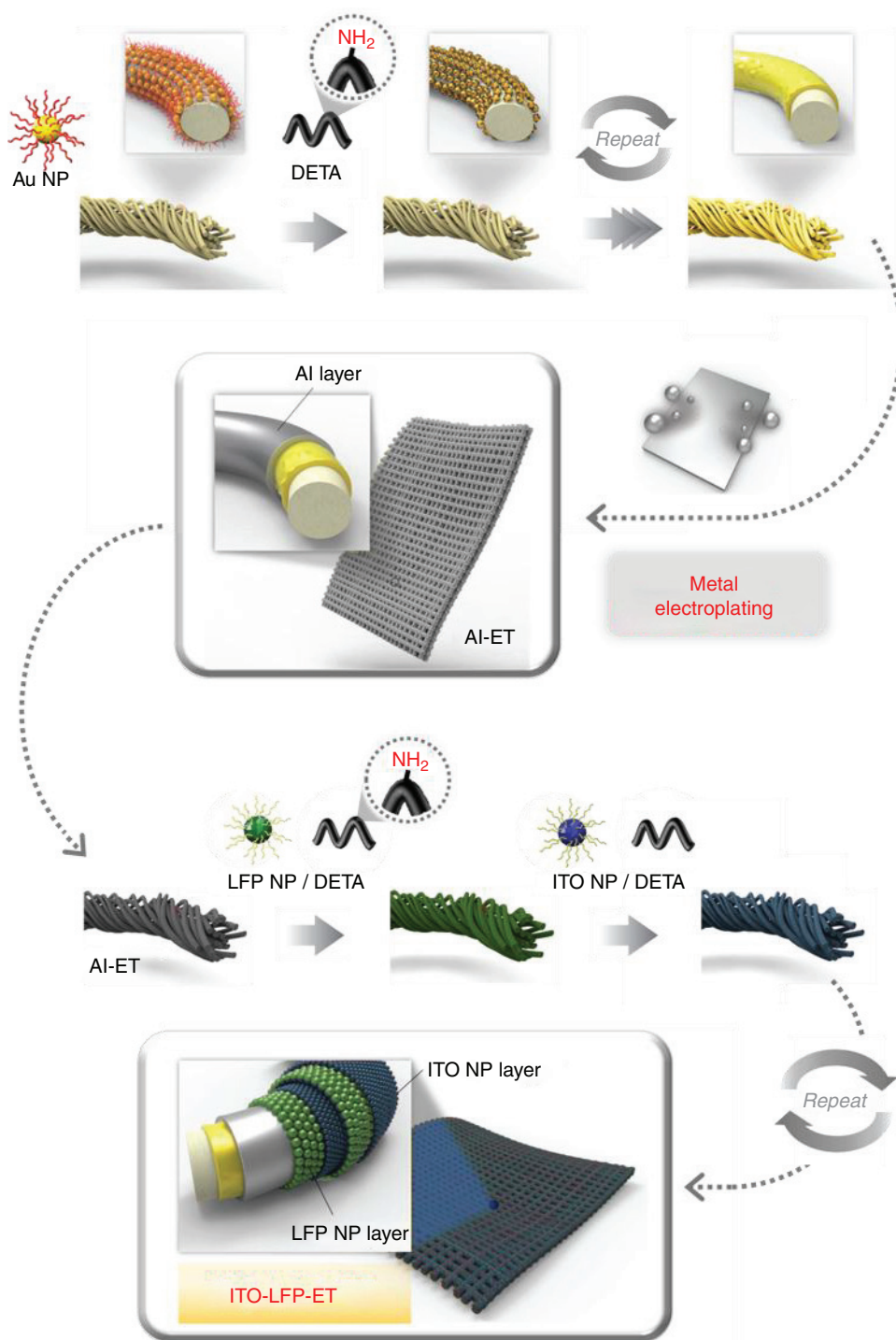


FIG. 1. Schematic illustration for the preparation of the textile-type battery cathodes based on small molecule linker-mediated layer-by-layer assembly and Al electroplating.

(DETA) onto polyester textiles via repetitive ligand exchange of TOA ligands with DETA linkers. Al electroplating was subsequently performed on the $(\text{Au NP/DETA})_n$ multilayer-coated polyester to complete the current collector, where n is the number of bilayers. In the same manner, polyester textiles can be prepared by coating with other

metal NPs, such as Cu and Ag NPs, for Al electroplating. We first investigated the adsorption behavior of LbL-assembled $(\text{Au NP/DETA})_n$ multilayer films. For this investigation, ~ 8 nm diameter TOA-Au NPs in toluene (Fig. S1 in the [supplementary material](#)) and DETA in ethanol were sequentially LbL-assembled onto the substrates,

which were qualitatively and quantitatively analyzed through UV-vis spectroscopy, quartz crystal microbalance (QCM) measurements, cross-sectional field-emission scanning electron microscopy (FE-SEM), and Fourier transform infrared (FTIR) spectroscopy (Figs. S2 and S3 in the [supplementary material](#)). The alternating LbL deposition of TOA-Au NPs and DETA induces ligand exchange of the bulky TOA ligands ($M_w \sim 322 \text{ g mol}^{-1}$) bound to the surface of the Au NPs with the smaller DETA molecules ($M_w \sim 103 \text{ g mol}^{-1}$) due to the higher affinity of the Au NPs for the NH_2 groups of DETA. As shown in the FTIR spectra (Fig. S2 in the [supplementary material](#)), the first deposition of TOA-Au NPs onto a poly(ethylene imine) (PEI)-coated Si wafer (0.5 bilayers) produced C—H stretching peaks (at 2928 and 2856 cm^{-1}) originating from the long alkyl chains of the TOA ligands. However, the subsequent adsorption of DETA onto the outermost TOA-Au NP layer (1 bilayer) eliminated the C—H stretching peaks of TOA ligands, whereas the intensities of the N—H stretching (at 3300 cm^{-1}) and bending (at 1654 and 1554 cm^{-1}) peaks increased due to DETA adsorption. The subsequent adsorption of TOA-Au NPs onto the outermost DETA layer (1.5 bilayers) regenerated the C—H stretching peaks of TOA ligands. These results imply that the organic layer existing within the resultant TOA-Au NP/DETA multilayers is only one DETA layer without bulky TOA ligands and minimizes the separation distance between neighboring Au NPs.

We also calculated the separation distance between vertically adjacent Au NPs within the LbL-assembled multilayers using a density functional theory (DFT) investigation of model systems for DETA between Au layers (Fig. S4 in the [supplementary material](#)). In this case, the interparticle distance was estimated to be approximately 5.6–5.7 Å. When the distance between neighboring metal NPs with low cohesive energy (e.g., Au $\sim 3.81 \text{ eV/atom}$ and Ag $\sim 2.95 \text{ eV/atom}$) is below 5–6 Å, room-temperature metallic sintering was recently reported to be caused by reciprocal atom diffusion. Additionally, the sintering of these Au NP arrays was confirmed by the red-shifting and subsequent disappearance of the surface plasmon absorption peak of Au NPs with increasing bilayer number, as shown in the UV-vis spectra [Fig. S3(a) in the [supplementary material](#)]. Furthermore, these results suggest that the closely packed Au NP films can exhibit high electrical conductivity.

Based on this adsorption behavior, we prepared an Al-electroplated textile that could be used as a current collector for a LIB cathode. To this end, $(\text{Au NP/DETA})_n$ multilayers were first deposited onto 150 μm -thick polyester textiles, which allowed for strong hydrogen-bonding interactions with the NH_2 groups of DETA. With increasing bilayer number from 3 to 10 [Fig. 2(a)], the sheet resistance and electrical conductivity of the $(\text{Au NP/DETA})_n$ -coated polyester textiles changed from $7.21 \times 10^5 \Omega \text{ sq}^{-1}$ and $9.25 \times 10^{-5} \text{ S cm}^{-1}$ to 1.43 $\Omega \text{ sq}^{-1}$ and 46.6 S cm^{-1} (including the thickness of the insulating polyester textile). Although further deposition of TOA-Au NP/DETA multilayers increased the electrical conductivity of the textile, we confirmed that the electrical properties (sheet resistance $\sim 300 \Omega \text{ sq}^{-1}$ and conductivity $\sim 0.37 \text{ S cm}^{-1}$) of the 4-bilayer multilayers were sufficiently suitable for metal electroplating based on a galvanostatic two-electrode system [Fig. 2(b)].

B. Metal electroplating onto LbL-assembled Au NP-coated textile

Prior to Al electroplating, Ni electroplating was performed on the $(\text{Au NP/DETA})_4$ multilayer-coated polyester textiles from an aqueous

solution to provide sufficient electrical conductivity during ionic liquid-mediated Al electroplating since the ionic liquid has low ionic conductivity (Fig. S5 in the [supplementary material](#)). The Al electroplating step was conducted using an ionic liquid rather than an aqueous solution because metals with a low standard reduction potential such as aluminum (-1.66 V) tend to react strongly with water to form a passivating oxide layer on the surface. The effective coating of electroplated Al onto textile was confirmed by x-ray diffraction (XRD) and x-ray photoelectron spectroscopy (XPS) (Fig. S6 in the [supplementary material](#)). Since Al current collectors have been used for commercial LIB cathodes, highly porous Al-electroplated textiles are very significant for the development of textile battery electrodes with high areal performance. To our knowledge, our approach is the first attempt at an Al-based textile cathode. By increasing the bilayer number of the predeposited Au NP/DETA from 4 to 10, the sheet resistance of the Al-electroplated textile decreased from 0.025 to 0.017 $\Omega \text{ sq}^{-1}$, and the electrical conductivity increased from 2350 to 3400 S cm^{-1} with an electroplating current density of 120 mA cm^{-2} for 10 min [Fig. 2(b)]. The remarkable electrical conductivities of the Al-ETs outperformed those of the textile-type electrodes reported to date. Although a higher current density and a longer electroplating time can considerably lower the sheet resistance of the Al-ET (Fig. S7 in the [supplementary material](#)), the Al electroplating conditions of the Ni-electroplated $(\text{Au NP/DETA})_4$ -coated polyester textiles (i.e., Ni-ETs) were controlled at a current density of 120 mA cm^{-2} for 10 min, taking into account the process efficiency and the Ni-ET conductivity. In this case, the thicknesses of the electroplated Ni sublayer and Al layer were approximately 0.28 μm and 1.78 μm , respectively (Fig. S8 in the [supplementary material](#)). In addition to the electrical conductivity (Fig. S7 in the [supplementary material](#)), the thickness of the Al layer can also be adjusted by tuning the electroplating time (Fig. S9 in the [supplementary material](#)). Moreover, the presence of both the LbL-assembled Au NP multilayer and the Ni layer induced conformal Al coating and preserved the porous fibril structure of the polyester textile after electroplating, allowing the utilization of the high surface area of the porous substrate as active sites [Fig. 2(c) and Fig. S10 in the [supplementary material](#)]. In addition to the TOA-Au NPs, TOA-Cu NPs (Fig. S11 in the [supplementary material](#)), and TOA-Ag NPs (Fig. S12 in the [supplementary material](#)) have also been successfully LbL-assembled with DETA for Al electroplating.

A notable advantage of our approach is that, despite the use of only 4 bilayers of metal NPs, the resultant electrodeposited textile electrode can exhibit bulk metal-like electrical conductivity while maintaining the highly porous structure of the native polyester textile without metal agglomeration. To further investigate the electrical transport, the electrical resistivity of the Al-ETs was measured with a physical property measurement system by increasing the temperature from 2 K to 300 K at a heating rate of 10 K/min [Fig. 2(d)]. The electrical resistivity linearly increased as the temperature increased, which is a typical metallic characteristic. In other words, the temperature coefficient (α) in the relation shown in Eq. (1) was positive, showing the electrical behavior of metal. The relation is expressed as follows:^{14,47}

$$\Delta R/R_0 = \alpha \Delta T, \quad (1)$$

where ΔR is the change in resistance from R_0 (Ω), R_0 is the resistance at 0 K (Ω), α is the temperature coefficient (K^{-1}), and T is the absolute

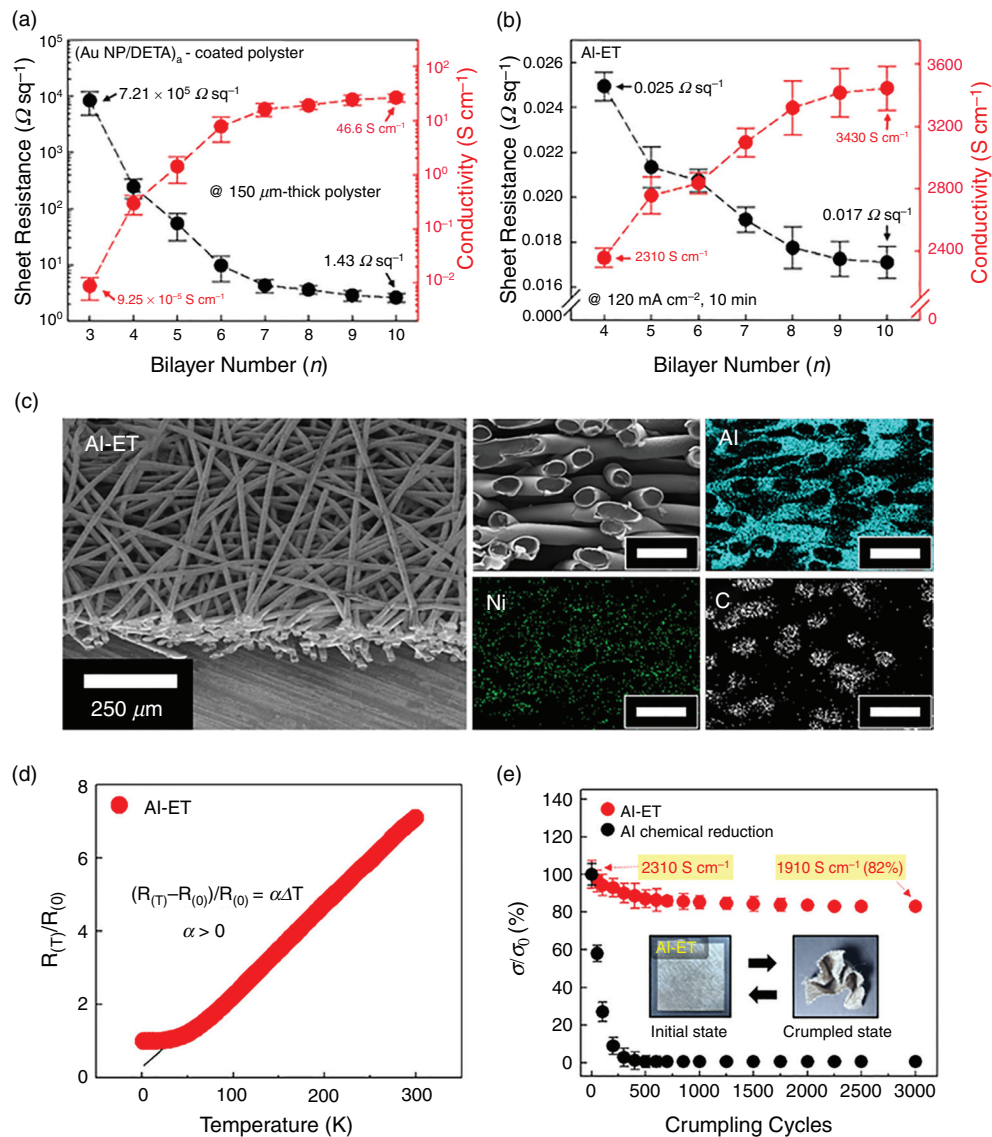


FIG. 2. Preparation and physical properties of Al electroplated textiles. (a) Sheet resistances and electric conductivities of the $(\text{Au NP/DETA})_n$ multilayer-coated polyester textile as a function of the bilayer number (n). (b) Sheet resistances and electric conductivities of the Al electroplated $\text{Ni}/(\text{Au NP/DETA})_n$ -polyester textile as a function of the bilayer number (n). (c) Tilted and cross-sectional (inset) FE-SEM images of the Al-ET [i.e., $\text{Al}/\text{Ni}/(\text{Au NP/DETA})_4$ -polyester] [scale bar, 250 and $50 \mu\text{m}$ (inset)] (right), and EDS mapping images of Al-ET (scale bar, $50 \mu\text{m}$) (right). (d) The resistance $[R(T)/R(0)]$ vs temperature (K) of Al-ET. (e) Mechanical stability tests for the Al-ET prepared from the Al electroplating approach and the chemical reduction of Al precursors as a function of the crumpling cycling number.

temperature (K). Additionally, the electrical transport behavior of the Al-ETs was found not to follow the hopping conduction model (Fig. S13 in the [supplementary material](#)), which can be expressed by the following equation:⁴⁸

$$\sigma = \sigma_0 \exp(-A/T^{1/(d+1)}), \quad (2)$$

where σ is the conductivity at T K, σ_0 is the conductivity at 0 K, A is a constant, T is the absolute temperature, and d is the dimensionality ($d = 3$ in the hopping mechanism).

The electroplated textile electrodes maintained 82% of the initial electrical conductivity and mechanical flexibility even under the repeated mechanical strain of 3000 crumpling cycles [Fig. 2(e)]. In contrast, the Al textile electrodes prepared following the reported chemical reduction approach²⁹ lost most of their electrical conductivity after only 75 crumpling cycles due to the formation of the relatively rigid Al layer (Fig. S14 in the [supplementary material](#)) including a large amount of organic impurities. Moreover, the conductivity change of Al-ET was investigated as a function of bending cycles, and it maintained 92.3% of the initial electrical conductivity after 5000 bending cycles [bending radius (R)

~1.5 mm] (Fig. S15 in the [supplementary material](#)). Therefore, the retention of electrical properties of LbL-assembly-assisted electroplated textiles after repeated mechanical deformation is superior to those of various other conductive textiles that have been prepared by electroless plating processes, physical adsorption processes,^{25–28} and/or traditional LbL assembly.^{33,45–48} Briefly, Al-electroplated textiles as a current collector were successfully fabricated using LbL-assembled metal NP multilayers and subsequent Ni/Al electroplating, which exhibited excellent mechanical properties and bulk Al-like electrical properties.

C. LFP NP-based multilayers onto Al-electroplated textile

LFP NPs, with diameters of ~35 and 7 nm ITO NPs were LbL-assembled onto Al-ETs (Fig. 1). To this end, oleylamine (OA)-stabilized LFP NPs (i.e., OA-LFP NPs) with high crystallinity were newly synthesized through the modification of synthetic methods reported by other research groups^{49,50} [Fig. 3(a) and Fig. S16 in the [supplementary material](#)]. LFP is a cathode material of LIBs with an olivine crystal

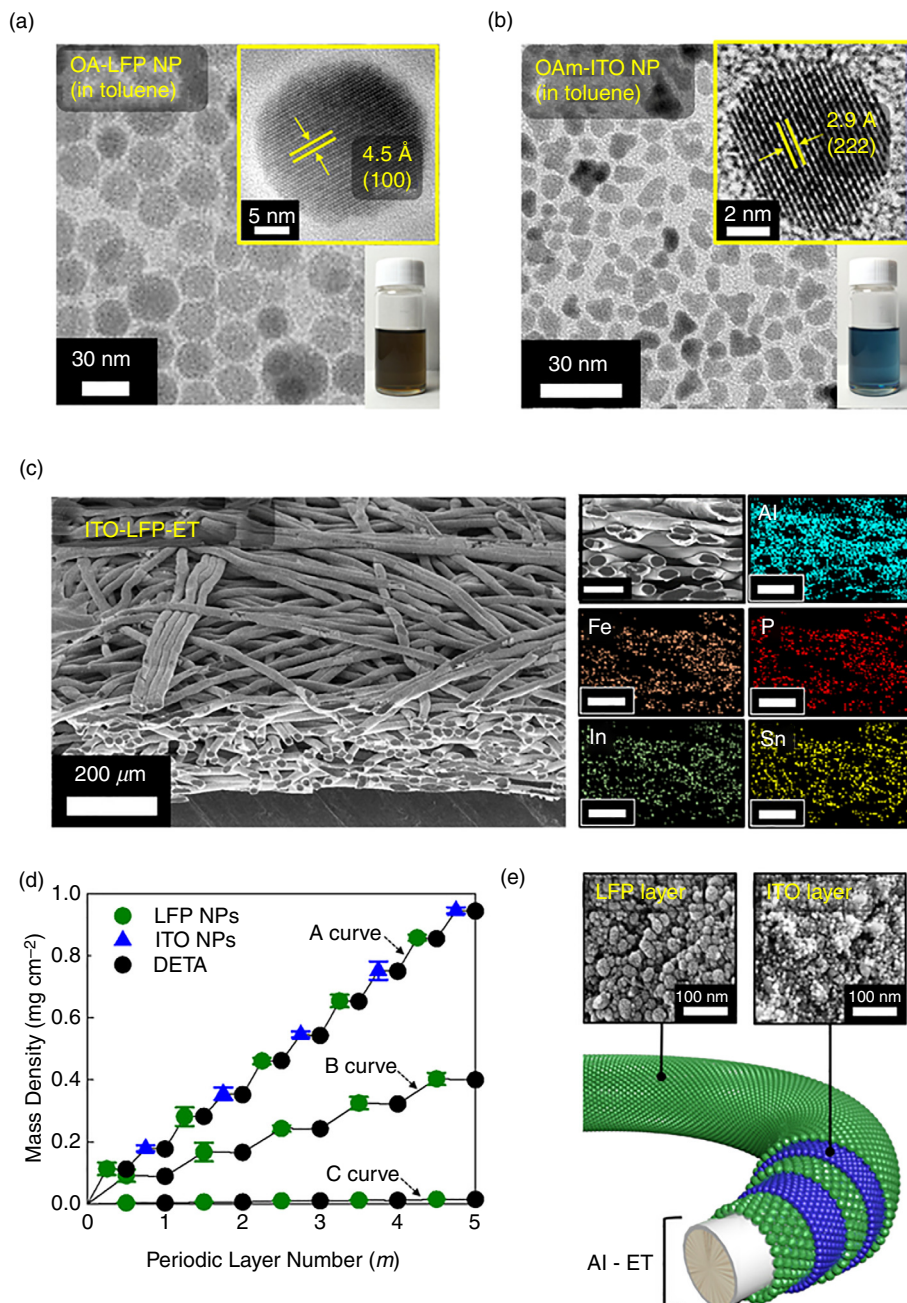


FIG. 3. Preparation and physical properties of LFP NP-based Al electroplated textiles. (a) HR-TEM images of OA-LFP NPs and photographic image of highly concentrated OA-LFP NP solution (in toluene). (b) HR-TEM images of OAm-ITO NPs and photographic image of highly concentrated OAm-ITO NP solution (in toluene). (c) Tilted and cross-sectional (inset) FE-SEM images of the ITO-LFP-ET [i.e., (LFP NP/DETA/ITO NP/DETA)_m/Al-ET] [scale bar, 200 and 50 μm (inset)] (right), and EDS mapping images of the ITO-LFP-ET (scale bar, 50 μm) (right). (d) Loading mass density of the (LFP NP/DETA/ITO NP/DETA)_m multilayers deposited onto Al-ET (A curve), (LFP NP/DETA)_m multilayers deposited onto Al-ET (B curve), and (LFP NP/DETA)_m multilayers deposited onto nonporous Al foil (C curve). (e) FE-SEM images and scheme of ITO-LFP-ET.

structure that exhibits a high specific capacity of $\sim 170 \text{ mA h g}^{-1}$. Conventional LFP particles with bulky sizes (from a few hundred nanometers to a few micrometers) have poor dispersion stability in organic media.^{51,52} However, the newly synthesized OA-LFP NPs showed high colloidal stability in toluene due to the attached organic ligands as well as their small size. Additionally, highly dispersible OAm-ITO NPs with diameters of approximately 7 nm were also prepared in the same organic media [Fig. 3(b)]. OAm-ITO NPs were used to enhance the charge transfer between neighboring LFP NPs, which have poor electrical conductivity.^{53,54} Like the TOA-Au NPs, these OA-LFP NPs and OAm-ITO NPs can be LbL-assembled with DETA through the above-mentioned ligand exchange reaction (Fig. S17 in the [supplementary material](#)),^{14,15,44,53–55} allowing coating of Al-ETs without NP agglomeration. Through the deposition of (LFP NP/DETA/ITO NP/DETA)_m multilayers onto Al-ETs, the LFP NPs and ITO NPs were homogeneously and densely distributed over the entirety of the textile electrodes, as confirmed by FE-SEM and energy dispersive x-ray spectroscopy (EDS) [Fig. 3(c)]. Moreover, TOA-Au NPs could be periodically incorporated into the (LFP NP/DETA)_m multilayers as conductive NPs instead of OAm-ITO NPs and, thus, could also enhance the charge transfer within the resultant LFP NP-based ET electrodes. Hereafter, the (LFP NP/DETA/ITO NP/DETA)_m-coated Al-ET, (LFP NP/DETA/Au NP/DETA)_m-coated Al-ET, and (LFP NP/DETA)_m-coated Al-ET will be abbreviated as ITO-LFP-ET, Au-LFP-ET, and LFP-ET, respectively.

First, to quantitatively investigate the mass loading density of the respective components according to the number of periodic multilayers (*m*), we analyzed ITO-LFP-ET (substrate size $\sim 1 \times 1 \text{ cm}^2$) with increasing layer number [Fig. 3(d)]. In this system, the mass loading densities of LFP NPs and ITO NPs were measured to be ~ 0.109 and $\sim 0.0796 \text{ mg cm}^{-2}$ per layer, respectively. In addition, the mass loading density of LFP NPs per layer in ITO-LFP-ET was slightly higher than that in LFP-ET ($\sim 0.0821 \text{ mg cm}^{-2}$) and Au-LFP-ET ($\sim 0.0936 \text{ mg cm}^{-2}$) (Fig. S18 in the [supplementary material](#)). For electrochemical evaluation, the mass loading densities of LFP NPs in ITO-LFP-ET, Au-LFP-ET, and LFP-ET were standardized by adjusting the periodic layer number. Notably, the mass loading density of the LFP NP multilayers adsorbed on the Al-ETs was ~ 27.5 times that of multilayers LbL assembled on nonporous Al foils, which was expected to significantly improve the areal capacity of the electrodes [Fig. 3(d)]. Furthermore, the FE-SEM images displayed in Fig. 3(e) show that the LFP NPs and ITO NPs were uniformly and densely coated on the outermost DETA layer coated on the substrate without agglomeration. Although TOA-Au NPs can also be used as the conductive NPs instead of OAm-ITO NPs, the Au NPs adsorbed through the ligand exchange reaction between the TOA ligands and DETA linker exhibit room-temperature metallic fusion, as described previously⁴⁴ (Figs. S19 and S20 in the [supplementary material](#)). Considering that the intercalation redox mechanism of LFP is governed by the ion diffusion kinetics of Li ions,⁵⁶ the fused Au NPs on the porous LFP NP multilayer-based electrodes would partially restrict ion transport within the interior of the electrodes during electrochemical operations. Because of this phenomenon, the metal oxide ITO NPs were used as a conductive filler to enhance the charge transport within the electrodes, despite their relatively low electrical conductivity compared to Au NPs.

D. Electrochemical performance of LFP NP-based textile battery electrode

Based on these results, we examined the electrochemical performances of ITO-LFP-ET, Au-LFP-ET, and LFP-ET as cathodes in LIBs using galvanostatic charge-discharge (GCD) measurements and electrochemical impedance spectroscopy (EIS). The total mass loading density of LFP NPs inserted within the respective multilayers was varied between 0.5 and 8 mg cm^{-2} by controlling the number of periodic layers. First, GCD tests were performed to clarify the charge-storage mechanism and performance of LFP NPs in the potential range of 2.0–4.0 V vs Li/Li⁺ at 0.1 C. The GCD curves of ITO-LFP-ET and Au-LFP-ET with LFP NP mass loading densities of ~ 2 and $\sim 8 \text{ mg cm}^{-2}$ showed typical charge-discharge plateaus around 3.4 V (vs Li/Li⁺) corresponding to the lithium extraction and insertion of the LFP NP host [Figs. 4(a) and 4(b)]. In contrast, the GCD curves of LFP-ET did not show any plateaus and exhibited poor electrochemical performance mainly due to the insulating nature of the LFP NPs (LiFePO₄ electrical conductivity $\sim 10^{-9} \text{ S/cm}$) (Fig. S21 in the [supplementary material](#)). Additionally, we also confirmed that the CV curve of ITO-LFP-ET exhibited typical anodic and cathodic peaks around 3.4–3.5 V, and on the other hand, the CV curve of LFP-ET did not show any peak (Fig. S22 in the [supplementary material](#)). For ITO-LFP-ETs, the areal capacities were 0.329 and $1.07 \text{ mA h cm}^{-2}$ for LFP NP mass loading densities of ~ 2 and $\sim 8 \text{ mg cm}^{-2}$, respectively. Moreover, we investigated the GCD curves of (ITO NP/DETA)_m-coated Al-ET for measuring the areal capacity of ITO NPs. In this case, the mass loading density of ITO NP contained in ITO-ET was measured to be approximately 5.8 mg cm^{-2} , which corresponded to that of ITO NPs in ITO-LFP-ET with LFP NP mass loading of 8 mg cm^{-2} . The areal capacity of (ITO NP/DETA)_m-coated Al-ET was estimated to be only $0.0481 \text{ mA h cm}^{-2}$ at 0.1 C (only 4.5% of the total areal capacity of ITO-LFP-ET) (Fig. S23 in the [supplementary material](#)). These results imply that the incorporated ITO NPs mainly operate as a conductive enhancer rather than energy storage materials within our electrode.

The specific capacity of ITO-LFP-ET slightly decreased as the mass loading density of LFP NPs was increased due to the increased electronic and ionic resistances, but the areal capacity increased almost linearly by 3.25 times when the mass loading density of LFP NPs increased from 2 to 8 mg cm^{-2} [Fig. 4(c) and Fig. S24 in the [supplementary material](#)]. In contrast to ITO-LFP-ET, the areal capacity of Au-LFP-ET only increased by 1.37 times when the 2 mg cm^{-2} LFP NP mass loading density was quadrupled, showing a sharp decline in the specific capacity. Although TOA-Au NPs have high electrical conductivity and improve the electron transport in the electrode, as mentioned above, the replacement of the bulky TOA ligands of incorporated Au NPs by small molecule linkers such as DETA results in a metallic fusion⁴⁴ that hinders facile ion transport and contributes to low capacities at high mass loading densities (Fig. S4 in the [supplementary material](#)). In addition, the GCD profiles of (LFP NP/DETA/ITO NP/DETA)₂₀-coated Al-ET and (LFP NP/DETA/ITO NP/DETA)₂₀-coated nonporous Al-plate were measured to investigate the effect of the high surface area of Al-ET on the areal capacity. In this case, the areal capacity of the Al-ET-based electrode was approximately 17.4 times higher than that of the nonporous Al-plate-based electrode (Fig. S25 in the [supplementary material](#)).

To gain more information about the electron and ion transport characteristics of the LFP NP-based ET electrodes, EIS of ITO-LFP-ET, Au-LFP-ET, and LFP-ET with LFP NP mass loading densities of $\sim 4 \text{ mg cm}^{-2}$ were investigated, as shown in Fig. 4(d). For each

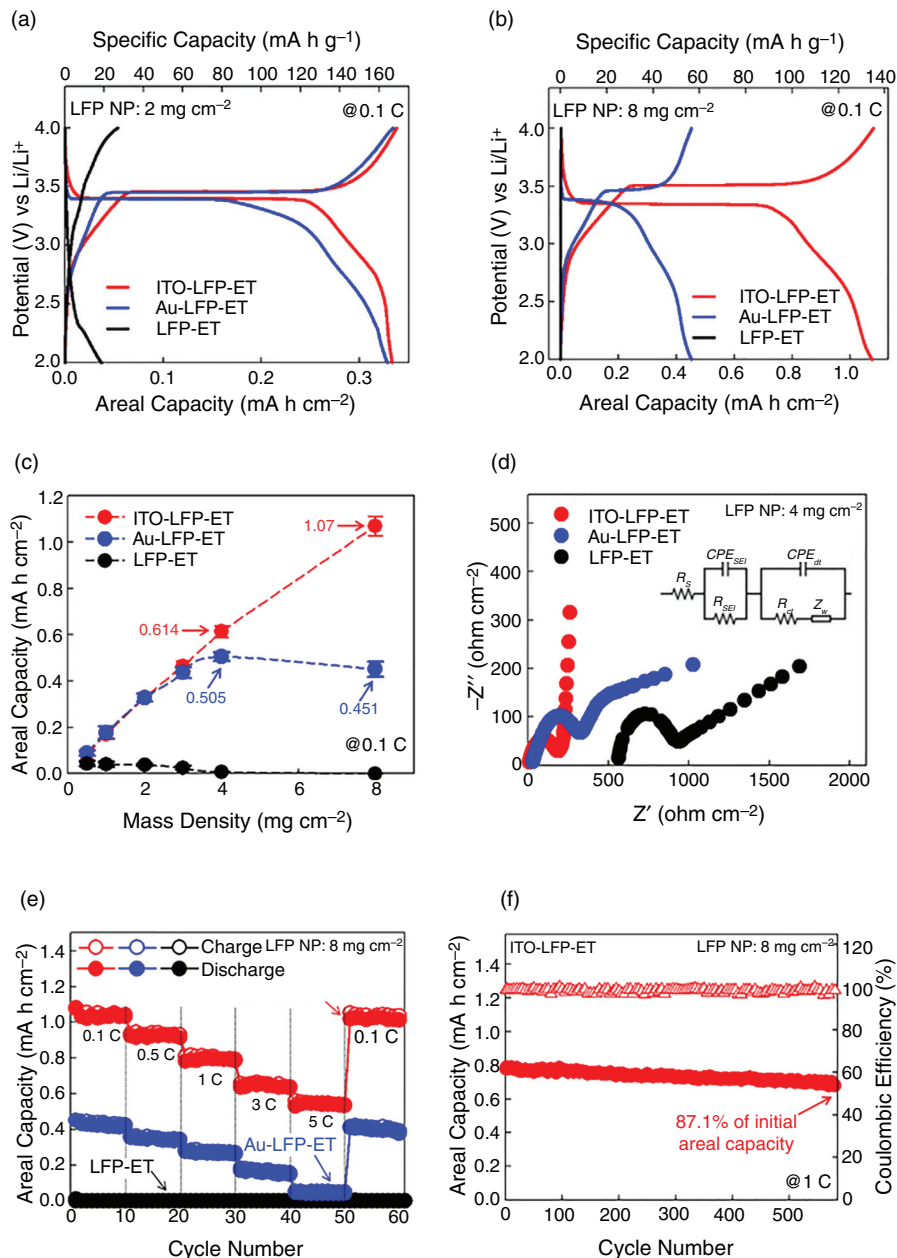


FIG. 4. Electrochemical measurements of LFP NP-based electrodes. GCD profiles of ITO-LFP-ET, Au-LFP-ET, and LFP-ET electrodes at 0.1 C. In these three different samples, the loading mass densities of LFP NP were fixed at (a) 2 mg cm⁻² and (b) 8 mg cm⁻². (c) Areal capacities of ITO-LFP-ET, Au-LFP-ET, and LFP-ET electrodes as a function of loading mass density of LFP NPs at 0.1 C. (d) Nyquist plots of ITO-LFP-ET, Au-LFP-ET, and LFP-ET electrodes with loading mass densities of LFP NP fixed at 4 mg cm⁻². The inset shows the representative equivalent circuit from the Nyquist plots. (e) Rate capability of ITO-LFP-ET, Au-LFP-ET, and LFP-ET electrodes (the loading mass densities of LFP NP ~8 mg cm⁻²) at varied current densities. (f) Cycling retention and Coulombic efficiency of ITO-LFP-ET electrodes with loading mass densities of 8 mg cm⁻² obtained at 1 C.

electrode, the Nyquist curve obtained from EIS measurements is composed of a depressed semicircular arc, which is related to the charge-transfer kinetics in the high-to-medium frequency region, and a linear tail, arising from the diffusion behavior of lithium ions in the low frequency region. In line with the trend in the capacitive behavior, the Nyquist curve of LFP-ET exhibited a high series resistance (R_s) of 562 Ω cm⁻², which includes the contact resistance at the electrolyte/electrode interface, the contact resistance at the material/current collector interface, the internal electrical resistance of the electrode, and a charge transfer resistance (R_{ct}) of 374 Ω cm⁻². The poor electrochemical performance of LFP-ET can be explained by the high resistance of

the LFP NP/DETA multilayers without a conductive filler (i.e., ITO NPs or Au NPs), which seriously hinders electron transport between the current collector and the redox active material. In comparison, ITO-LFP-ET and Au-LFP-ET exhibited lower R_s values of 35.2 Ω cm⁻² and 29.1 Ω cm⁻², respectively, due to the incorporation of conductive ITO NPs or Au NPs that improve electron transport.¹⁴ However, despite the slightly lower R_s of Au-LFP-ET than that of ITO-LFP-ET, Au-LFP-ET exhibited a larger semicircle than ITO-LFP-ET, implying a larger R_{ct} . In the case of Au-LFP-ET, the slow penetration of lithium ions due to the partially fused Au NPs surrounding the LFP NPs may contribute to the relatively large semicircle. These results

indicate that ITO-LFP-ET shows favorable charge transfer behavior compared to that within Au-LFP-ET and LFP-ET.

Additional analyses of the Warburg impedance, represented by the linear tail in the low frequency region, of ITO-LFP-ET, Au-LFP-ET, and LFP-ET were investigated to better understand the diffusion behavior of lithium ion transport within the three different electrodes⁵⁷ (Figs. S26 and S27 in the [supplementary material](#)). In this case, the diffusion coefficients (D) of Li in the respective electrodes were calculated from the Warburg impedance coefficient (σ_w) obtained from the slope of the linear tail in the Nyquist curve using the following equation (Fig. S27 in the [supplementary material](#)):⁵⁸

$$Z' = R_s + R_{ct} + \sigma_w \omega^{-0.5}, \quad (3)$$

$$D = 0.5 \left(\frac{RT}{AF^2 \sigma_w C} \right)^2, \quad (4)$$

where ω , R , T , A , F , and C are the angular frequency, the gas constant, the absolute temperature (K), the electrode area (cm^2), Faraday's constant (C mol^{-1}), and the molar concentration of ions in the electrolyte (mol l^{-1}), respectively. Based on this equation, the diffusion coefficients in ITO-LFP-ET, Au-LFP-ET, and LFP-ET were calculated to be 1.58×10^{-10} , 1.65×10^{-12} , and $4.75 \times 10^{-14} \text{ cm}^2 \text{ s}^{-1}$, respectively. The extremely low diffusion coefficient in LFP-ET is attributed to the high resistance due to the poor electrical conductivity of the LFP NP/DETA multilayers. These results also indicate that the nanoporous structure of the ITO-LFP multilayers, which do not exhibit metallic fusion, can effectively facilitate ion transport in the ITO-LFP electrode. In contrast, the numerous nanovoids (i.e., nanopores formed among NPs) within Au-LFP multilayers are partially blocked by the fused Au NPs, giving rise to a lower diffusion coefficient than that of ITO-LFP-ET despite the higher electrical conductivity of Au NPs. Therefore, the capacity loss ratio of Au-LFP-ET with sluggish ion transport grows with the increased total mass loading density of OA-LFP NPs and TOA-Au NPs. This large loss ratio thus can explain the gap between the areal capacity values of ITO-LFP-ET and Au-LFP-ET occurring at high mass loading densities of LFP NPs ($> 2 \text{ mg cm}^{-2}$).

We also investigated the rate capabilities of ITO-LFP-ET, Au-LFP-ET, and LFP-ET, as shown in Fig. 4(e). The areal capacities of LFP-ET, which has poor charge transfer, were extremely low regardless of the applied current density, as expected. In contrast, with the aid of conductive NPs, ITO-LFP-ET and Au-LFP-ET exhibited areal capacities of 1.07 and $0.451 \text{ mA h cm}^{-2}$ (initial discharge capacity recorded at 0.1 C), respectively. The current density was gradually increased from 0.1 (i.e., 0.136 mA cm^{-2}) to 0.5, 1, 3, and 5 C (i.e., 6.8 mA cm^{-2}), and the corresponding discharge areal capacity of ITO-LFP-ET progressively decreased from 1.07 to 0.925, 0.7817, 0.6368, and $0.531 \text{ mA h cm}^{-2}$ (i.e., 49.6% of the initial areal discharge capacity at 0.1 C) (Fig. S28 in the [supplementary material](#)). In contrast, a sharp decline in capacity was observed for Au-LFP-ET, showing only 11.0% ($0.0497 \text{ mA h cm}^{-2}$) capacity retention when the current density was increased from 0.1 to 5 C. As mentioned above, these results demonstrate the effect of the ion transport kinetics on the rate capabilities. That is, the facile charge transfer within the nanoporous ITO-LFP-ET electrode can allow a high charge-discharge rate, but the Au-LFP-ET electrode has a considerable capacity loss at high current densities due to its partial metallic fusion. In addition, when the current density was decreased to 0.1 C after 50 charge-discharge cycles, the areal capacity

of ITO-LFP-ET recovered up to $\sim 94.7\%$ of the average areal capacity measured in the initial 10 cycles.

We also investigated the cycling stability of ITO-LFP-ET with various mass loading densities of LFP NPs. As shown in Fig. 4(f) and Fig. S29 in the [supplementary material](#), the areal discharge capacities of ITO-LFP-ET with LFP NP mass loading densities of $\sim 8 \text{ mg cm}^{-2}$ were maintained at $\sim 87.1\%$ of the initial areal discharge capacity (i.e., $0.781 \text{ mA h cm}^{-2}$) after 580 charge-discharge cycles with a charge rate of 1 C. Additionally, the ITO-LFP-ETs maintained Coulombic efficiencies of $> 95.9\%$ throughout the 580 cycles regardless of the mass loading density. On the other hand, Au-LFP-ET exhibited 74.6% of its initial areal capacity after 420 charge-discharge cycles at 1 C (Fig. S30 in the [supplementary material](#)). These results emphasize that the charge-discharge performance of the LbL-assembled nanocomposite film composed of ITO NPs and LFP NPs can be maintained at a high mass loading (8 mg cm^{-2}) of active material after hundreds of cycles.

To assemble a full-cell LIB with the ITO-LFP-ET cathode, Fe_3O_4 NPs were LbL-assembled with tricarboxylic acid (TC) onto a Ni-ET as an anode (Fig. S31 in the [supplementary material](#)). As shown in Fig. S32 in the [supplementary material](#), the electrochemical performance of the $(\text{Fe}_3\text{O}_4 \text{ NP/TC})_m$ -coated Ni-ET (i.e., Fe_3O_4 -ET) with a mass loading density of Fe_3O_4 NP $\sim 1 \text{ mg cm}^{-2}$ was evaluated as a half-cell in the voltage range of 0–3 V. The full-cell LIB, composed of ITO-LFP-ET with a LFP NP mass loading density of $\sim 4 \text{ mg cm}^{-2}$ and Fe_3O_4 -ET with a Fe_3O_4 NP mass loading density of $\sim 1 \text{ mg cm}^{-2}$, exhibited an areal capacity of $0.584 \text{ mA h cm}^{-2}$ in the voltage range of 0.5–3.5 V, maintaining approximately 95% of the half-cell areal capacity of the ITO-LFP-ET (Fig. S33 in the [supplementary material](#)). Therefore, full-cell LIB assembly is possible because anode as well as cathode can be successfully manufactured through our approach.

Another notable benefit of our approach is that the geometric areal capacity of ET-based electrodes with high mechanical flexibility can be significantly enhanced by folding of the textile electrode as well as by simply increasing the number of LbL-assembled LFP NP layers [Fig. 5(a)]. The trade-off between higher loading amounts of active materials and the increasingly poor electrical conductivity and sluggish charge transport kinetics at greater loading densities acts as an unavoidable obstacle to increasing the areal capacity of LIB electrodes. Therefore, folding of the ET-based electrode can be an effective means to minimize this trade-off and increase the areal performance substantially at the same time.

To demonstrate the effectiveness of ET electrodes folded multiple times, the electrochemical performance of ITO-LFP-ET electrodes with a LFP NP mass loading density of 8 mg cm^{-2} was investigated as the folding number (i.e., the number of folds) was increased [Figs. 5(b)–5(e)]. The geometric areal capacity of ITO-LFP-ET increased almost proportionally as the folding number increased, exhibiting areal discharge capacities of 1.07, 1.94, and $3.28 \text{ mA h cm}^{-2}$ for folding numbers of 0, 1, and 2, respectively, at 0.1 C [Fig. 5(b)]. These results indicate that facile electron and ion transport are maintained even under mechanical deformation, such as folding. As shown in Fig. S34 in the [supplementary material](#), partial cracks in the folding edge area of the electroplated Al layer appeared after folding the Al-ET to 180° . However, since the cracks in this folded state were concentrated on the folding edge, the electrical properties of the Al-ET were stably maintained, since the Al-electroplated fibers with a high degree of interconnection and flexibility could maintain their conductive network

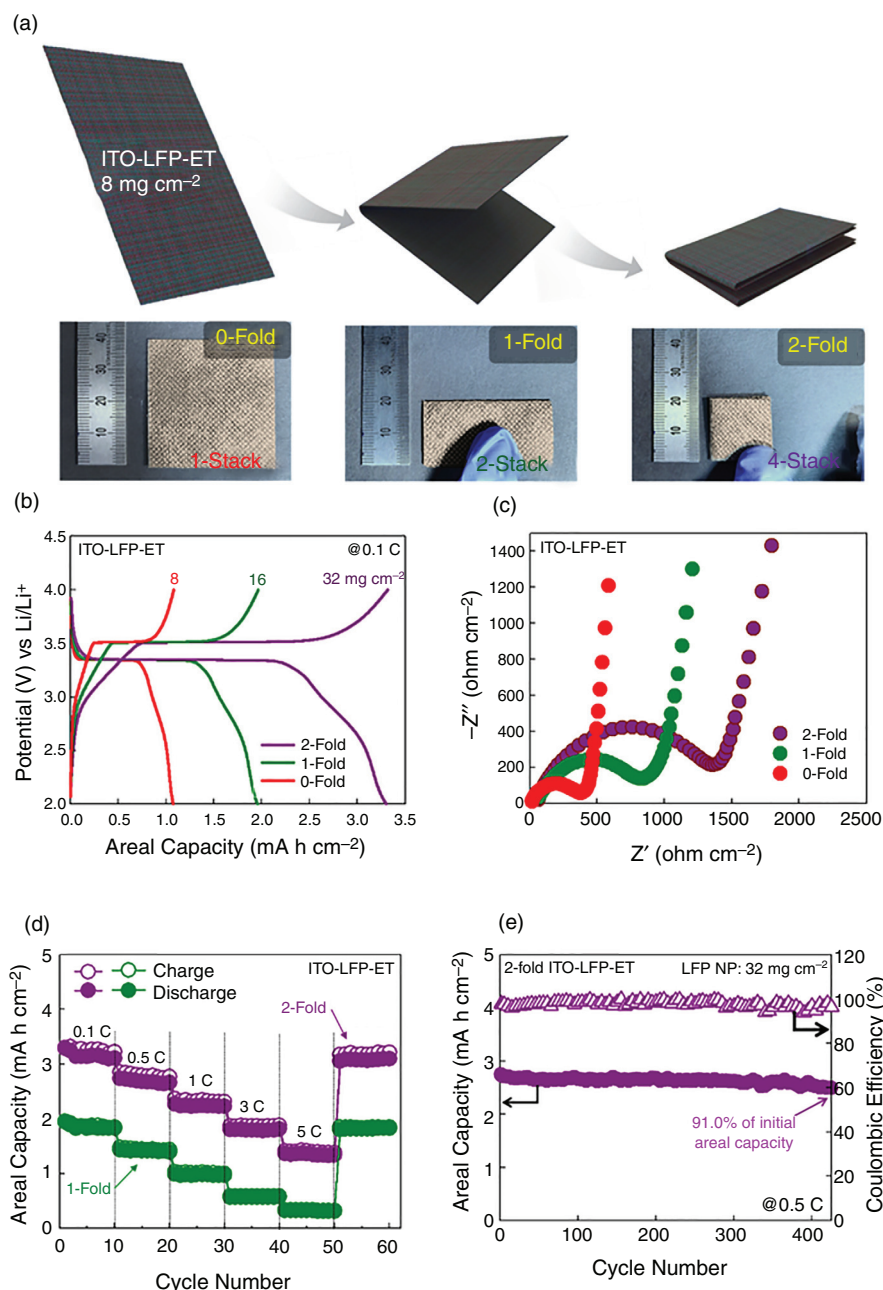


FIG. 5. Electrochemical measurements of folded LFP NP-based electrodes. (a) Scheme and photographic images of multi-foldable Al-ET-based electrodes. (b) GCD profiles of ITO-LFP-ET electrodes as a function of folding number (n -fold) at 0.1 C. With increasing the folding number from 0 to 2, the loading mass density of LFP NPs was increased from 8 to 32 mg cm⁻². (c) Nyquist plots of ITO-LFP-ET electrodes with 0-, 1-, and 2-folded number. (d) Rate capability of 1- and 2-folded ITO-LFP-ET electrode at varied current densities. (e) Areal capacities of 2-fold ITO-LFP-ET with the loading mass density of 32 mg cm⁻² at 0.5 C.

even under serious mechanical deformation [Fig. S34(b) in the [supplementary material](#)]. As shown in Fig. 5(c), the Nyquist curves of multiple folded ITO-LFP-ETs exhibited larger semicircles in the high-to-medium frequency region, indicating an increase in R_{ct} with folding number from 360 to 1292 Ω cm⁻² due to the increased total thickness of the electrodes (including ET thickness) per unit area. Considering that the areal mass density of LFP NPs is multiplicatively increased per folding, the mass density of LFP NPs within the 2-folded electrode is increased up to approximately 32 mg cm⁻². However, the R_s values of the 0-, 1-, and 2-folded electrodes were

almost maintained in the range of 15.7–65.8 Ω cm⁻², and these electrodes furthermore exhibited similar linear slopes in the low frequency region, indicating that the ion transport kinetics can be preserved despite the increase in the folding number.

Moreover, the 2-folded ITO-LFP-ET exhibited a good rate capability despite the significantly increased thickness of the overall electrode [Fig. 5(d) and Fig. S35 in the [supplementary material](#)]. Specifically, as the charge rate was increased from 0.1 (i.e., 0.544 mA cm⁻²) to 0.5, 1, 3, and 5 C (i.e., 27.2 mA cm⁻²), the areal discharge capacity gradually decreased from 3.28 to 2.73, 2.27, 1.81, and 1.36 mA h cm⁻² (i.e.,

41.4% of the initial areal discharge capacity at 0.1 C), respectively. When the charge rate was decreased to 0.1 C after 50 charge-discharge cycles, the areal capacity of ITO-LFP-ET returned to $3.08 \text{ mA h cm}^{-2}$ (average discharge capacity of 10 cycles at 0.1 C recorded after 50 cycles), which corresponded to $\sim 93.9\%$ of the average discharge capacity measured in the initial 10 cycles. Furthermore, we investigated the cycling stability of 2-folded ITO-LFP-ET, as shown in Fig. 5(e) and Fig. S36 in the supplementary material. In this case, the areal capacity of 2-folded ITO-LFP-ET still maintained 91% of the initial areal capacity with a high Coulombic efficiency of $>94.8\%$ after 420 cycles.

III. CONCLUSION

In this study, we demonstrated LbL-assembled NP-based LIB cathodes using 3D Al textile current collectors with remarkable areal capacity and good rate capability. Particularly, the use of ligand exchange LbL assembly and subsequent Ni electroplating to aid Al electroplating completely covered the insulating polyester fibrils within the textile with conductive Al while maintaining the highly porous structure of the pristine polyester textile without any metal aggregation or blockage of pores. Therefore, the formed Al-ET could be effectively used as a metal-like current collector in battery cathodes, which have been never reported to date. The alternating deposition of 35-nm LFP NPs and 7 nm conductive ITO NPs into the highly porous Al-ET using the same ligand exchange LbL assembly method resulted in an increase in the areal capacity of the electrode as well as facile charge transfer between neighboring LFP NPs. Furthermore, the folding of the ITO-LFP-ET electrode considerably enhanced the geometric areal capacity without significantly compromising the rate capability. Specifically, the mass loading density and the areal capacity of the 2-folded electrode were increased up to 32 mg cm^{-2} and $3.28 \text{ mA h cm}^{-2}$ (at 0.1 C), respectively. The introduced approach can be widely implemented in electrodes that require a large surface area, a metal-like conductivity, complementary interfacial interactions, and a controlled loading amount of active materials for various electrochemical device applications beyond battery electrodes.

IV. EXPERIMENTAL METHODS

A. Synthesis of TOA-Au NPs

TOA-Au NPs with diameters of approximately 8 nm and stabilized by TOA ligands were synthesized according to the Schiffrin method.^{59,60} Tetraoctylammonium bromide (TOABr) (2 mmol) was initially dispersed in 80 ml of toluene. Then, 30 mM gold(III) chloride trihydrate ($\text{HAuCl}_4 \cdot 3\text{H}_2\text{O}$, Sigma-Aldrich) dissolved in de-ionized water (30 ml) was added and vigorously stirred. After 10 min, 0.4 M NaBH_4 dissolved in de-ionized water (25 ml) was poured into the solution as a reducing agent and maintained for 3 h. Finally, the toluene phase was separated from the mixture and washed several times with H_2SO_4 (0.1 M, 95% purity, Daejung Chemicals), NaOH (0.1 M, 97%, Sigma-Aldrich), and pure de-ionized water to eliminate the residual reactants.

B. Synthesis of TOA-Cu NPs

TOA-Cu NPs with diameters of approximately 8 nm and stabilized by TOA ligands were synthesized according to the modified Brust-Schiffrin method. Copper(II) chloride dihydrate (0.3 mmol, $\text{CuCl}_2 \cdot 2\text{H}_2\text{O}$, $\geq 99.95\%$ trace metal basis, Sigma-Aldrich) dissolved in

7 ml of de-ionized water and TOABr (0.75 mmol) dispersed in 8 ml of toluene were mixed and vigorously stirred. Then, sodium thiosulfate powder (1.2 mmol, $\text{Na}_2\text{S}_2\text{O}_3$, 99%, Sigma-Aldrich) was poured into the solution. After 10 min, NaBH_4 dissolved in de-ionized water was added to the mixture as a reducing agent. Finally, the aqueous phase was discarded from the mixture, and the toluene phase was washed several times with 0.01 M HCl , 0.01 M NH_4OH , and pure de-ionized water in order to remove the residual reactants.

C. Synthesis of TOA-Ag NPs

Ag NPs stabilized with TOA ligands with diameters of approximately 8 nm were prepared through the modified Brust-Schiffrin method. Silver nitrate (0.9 mmol, AgNO_3 , Sigma-Aldrich) dissolved in 24 ml of de-ionized water and TOABr (2.25 mmol) dispersed in 24 ml of toluene were mixed and vigorously stirred in a water bath at 40°C . $\text{Na}_2\text{S}_2\text{O}_3$ (3.6 mmol) was added to the mixture and maintained for 10 min. Subsequently, the toluene phase was separated from the mixture, and the reaction flask was replaced by another empty flask. Then, 19.2 mM NaBH_4 dissolved in de-ionized water was sequentially added to the mixture. After 10 min of reaction, the solution was washed several times with 0.01 M HCl , 0.01 M NH_4OH , and pure de-ionized water to eliminate the residual reactants.

D. Synthesis of OA-LFP NPs

OA-LFP NPs, measuring $\sim 35 \text{ nm}$, in toluene were synthesized through a solvothermal method. Thirty milliliters of oleylamine (OAm) and 28 ml of oleic acid (OA) were initially poured into a three-neck flask and stirred under vacuum for 30 min. Then, 4 mmol iron(II) diacetate [$\text{Fe}(\text{CO}_2\text{CH}_3)_2$, Sigma-Aldrich] and 4 mmol lithium acetate (LiOOCCH_3 , 99.95%, Sigma-Aldrich) were added to the mixture. After that, the mixture was rapidly heated to 150°C under an argon atmosphere and then cooled to 70°C after the color of the solution changed to green. Then, 0.28 ml of phosphoric acid (H_3PO_4 , crystals, 99.999+%, Sigma-Aldrich) was injected into the flask and stirred under vacuum. After 30 min, the solution was heated to 350°C under an argon atmosphere and maintained for 2 h. The resultant mixture was washed with acetone and ethanol through centrifugation. Finally, the OA-LFP NPs were dispersed in toluene.

E. Synthesis of OAm-ITO NPs

All the chemicals used in the synthesis of OAm-ITO NPs were purchased from Sigma-Aldrich. OAm-ITO NPs with diameters of approximately 7 nm was stabilized with oleylamine (OAm) and dispersed in toluene using a method reported by Kanehara *et al.*⁶¹ Briefly, 3.24 mmol of indium(III) acetate, 30 ml of dioctyl ether, 0.36 mmol of tin 2-ethylhexanoate, and 10.8 mmol of octanoic acid was poured into the three-neck flask and purged with argon gas. Next, the flask was switched to a closed system and the mixture was vigorously stirred for 1 h at 150°C . Then, the mixture was heated to 280°C . After 2 h, the solution was cooled and washed with acetone through centrifugation. Finally, the OAm-ITO NPs were dispersed in toluene.

F. Synthesis of OA- Fe_3O_4 NPs

All the chemicals used in the synthesis of OA- Fe_3O_4 NPs were purchased from Sigma-Aldrich. OA- Fe_3O_4 NPs, measuring 8 nm in

toluene was prepared according to previously reported protocol.⁶² Briefly, 20 ml of benzyl ether was poured into the three-neck flask and 2 mmol of iron(III) acetylacetonate, 10 mmol of 1,2-hexadecanediol, 6 mmol of oleic acid, and 6 mmol of oleylamine were added. The mixture was heated to 200 °C under argon atmosphere and maintained for 2 h. Then, the flask was switched to a closed system and the solution was heated to 300 °C with reflux. After 1 h, the mixture was cooled and washed with ethanol and acetone through centrifugation. Finally, the dark brown solution of OA-Fe₃O₄ NPs in toluene was prepared.

G. Preparation of metal NP-assembled textiles

Dispersions of the hydrophobic metal NPs (TOA-Au, TOA-Ag, TOA-Cu) in toluene (5 mg ml⁻¹) and of DETA in ethanol (1 mg ml⁻¹) were prepared for the fabrication of metal NP-assembled textiles. The polyester textile substrate was initially dipped into poly(ethylene imine) (PEI) in ethanol for 10 min. Next, the metal NPs were deposited onto the PEI-coated substrate by dipping them into the hydrophobic metal NP solution for 10 min and cleaning with pure toluene for detachment of the weakly bound NPs. Then, the substrate was dipped into the DETA solution for 10 min to induce a ligand exchange reaction, replacing the hydrophobic alkyl ligand of metal NPs with DETA, and cleaned with pure ethanol. These procedures were repeated several times to form a (metal NP/DETA)_n multilayer-coated textile with sufficient conductivity to be electroplated.

H. Preparation of electroplated textiles

The (metal NP/DETA)_n multilayer-coated textile substrate and a Ni foil (Nickel foil, 99.9+%, Sigma-Aldrich) were connected to an electroplating circuit as the cathode and anode, respectively. The electrodes were dipped into the Ni electroplating solution, and electroplating was conducted for 5 min at 250 mA cm⁻² using a power supply. The Ni electroplating solution consisted of 240 g l⁻¹ nickel(II) sulfate hexahydrate (NiSO₄·6H₂O, Sigma-Aldrich), 45 g l⁻¹ nickel(II) chloride hexahydrate (NiCl₂·6H₂O, Sigma-Aldrich), 30 g l⁻¹ boric acid (H₃BO₃, Sigma-Aldrich) and de-ionized water.^{63–65} The Ni-electroplated textile (i.e., Ni-ET) was cleaned with de-ionized water and dried in a vacuum oven at 120 °C. Then, the Al electroplating solution, which consisted of 60 ml of {[EMIm]Cl-AlCl₃} (1-ethyl-3-methylimidazolium chloride-aluminum chloride, (C₆H₁₁ClN₂)₂-(AlCl₃)₃, Sigma-Aldrich) and 40 ml of toluene was prepared under an argon atmosphere.^{66–68} In the same manner as Ni electroplating, the dried Ni-ET and an Al foil (aluminum foil, 99+%, Nilaco Corporation) were connected to the electroplating circuit and dipped into the Al electroplating solution. Then, galvanostatic electrodeposition was conducted on the connected Ni-ET using an Ivium-n-stat (Ivium Technologies). After electroplating, the Al-ET was sequentially washed with ethanol and de-ionized water. Finally, the Al-ET was dried in a vacuum oven at 120 °C.

I. Preparation of Al textile through chemical reduction

Aluminum chloride (AlCl₃), lithium aluminum hydride (LiAlH₄; LAH), dibutylether [O(C₄H₉)₂], and titanium isopropoxide catalyst [Ti(O-*i*-Pr)₄] were purchased from Aldrich Chemical.²⁹ First, the Al precursor composite solution {AlH₃[O(C₄H₉)₂]} was prepared by stirring a mixture of 20 mmol of AlCl₃, 60 mmol of LAH, and 50 ml of

dibutylether for ~1 h at 75 °C. The resulting gray slurry was filtered, and the cleared solution was used as an Al precursor composite solution. Next, catalytic treatment was conducted on a textile substrate. The textile substrate was placed on a hot plate and preheated to 110 °C under an Ar atmosphere. After that, 10 μl of the Ti(O-*i*-Pr)₄ catalyst was dropped on the hot plate and covered with a glass chamber for 10 min to expose the textile substrate to the fumed catalyst. Finally, the exposed textile was immersed into the Al precursor composite solution for 4 h.

J. Preparation of LFP NP-based electroplated textile electrodes

For the preparation of LFP NP-based ET electrodes, the Al-ETs were initially dipped into PEI in ethanol (1 mg ml⁻¹). In the case of LFP-ET electrodes, OA-LFP NPs in toluene (10 mg ml⁻¹) and DETA (1 mg ml⁻¹) in ethanol were alternately deposited onto the PEI-coated Al-ET, inducing ligand exchange reactions, with a dipping time of 10 min for each component. The washing (toluene washing after OA-LFP NP solution dipping and ethanol washing after DETA solution dipping) and drying processes were followed after each dipping process. The dipping and washing procedures were repeated until the target bilayer number was reached.

For the preparation of the ITO-LFP-ET and Au-LFP-ET electrodes, the PEI-coated Al-ET was subsequently dipped into OA-LFP NPs in toluene (10 mg ml⁻¹), DETA in ethanol (1 mg ml⁻¹), conductive NPs (i.e., OAm-ITO NPs or TOA-Au NPs) in toluene (10 mg ml⁻¹), and DETA in ethanol (1 mg ml⁻¹) with a dipping time of 10 min for each component. In the same manner as the above-mentioned procedure, the washing and drying processes were followed in order after each dipping process. These series of processes were repeated until the target periodic layer number was reached.

K. Preparation of Fe₃O₄ NP-based electroplated textile electrodes

For the preparation of Fe₃O₄ NP-based ET electrodes, the Ni-ETs were initially dipped into PEI in ethanol (1 mg ml⁻¹). OA-Fe₃O₄ NPs in toluene (10 mg ml⁻¹) and TC (1 mg ml⁻¹) in ethanol were alternately deposited onto the PEI-coated Ni-ET with a dipping time of 10 min for each component. The washing (toluene washing after OA-Fe₃O₄ NP solution dipping and ethanol washing after TC solution dipping) and drying processes were followed after each dipping process. The dipping and washing procedures were repeated until the target bilayer number was reached.

L. Characterization

The HR-TEM data of synthesized NPs were obtained using a Technai 20 instrument (FEI). UV-vis spectra of the LbL-assembled multilayers were monitored with a Lambda 35 instrument (Perkin Elmer) within a scan range of 200–800 nm via LbL deposition on quartz glass slides. The quantitative deposition of the LbL-assembled multilayers was monitored through QCM (QCM 200, SRS) measurements. The mass loading of each layer was calculated from the measured frequency difference based on the Sauerbrey equation.⁶⁹ Fourier transform infrared spectra of the multilayers were analyzed in specular mode with a resolution of 4 cm⁻¹ using a CARY 600 spectrometer (Agilent Technologies) and the obtained data were plotted with

spectral analysis software (OMNIC, Nicolet). FE-SEM and EDS mapping data were obtained using an S-4800 instrument (Hitachi). The temperature-dependent electrical properties of the AL-ETs were measured with a physical property measurement system (PPMS-9, Quantum Design) within a temperature range of 2 to 300 K.

M. Electrochemical measurements

The electrochemical investigations for all electrodes were conducted with 2032-coin cells (CR2032, MTI Korea) using a WBCS3000 multichannel workstation. All cells were assembled in an argon-filled glovebox (MBraun, $O_2 < 0.1$ ppm, $H_2O < 0.1$ ppm), typically with Li foils as both counter and reference electrodes, though some cells utilized the Fe_3O_4 -ET anodes. The size of all fabricated electrodes was fixed at $1\text{ cm} \times 1\text{ cm}$ (1 cm^2). The liquid electrolyte was 1 M $LiPF_6$ dissolved in a mixture of ethylene carbonate (EC) and dimethyl carbonate (DMC) with a volume ratio of 3:7. The galvanostatic charge-discharge performance was evaluated with a ZIVE mp2 (WonATech, Republic of Korea) in the voltage range of 2.0 to 4.0 V (vs Li/Li^+) at room temperature. EIS measurements were conducted in the frequency range of 100 kHz to 0.1 Hz with a perturbation amplitude of 0.01 mV.

SUPPLEMENTARY MATERIAL

See the [supplementary material](#) for the UV-vis spectra and TEM image of materials, FTIR spectra and QCM data of assembled film, additional SEM data, XRD data, XPS data, mechanical stability tests, electrochemical performances of the textile-based electroplated electrode, characterization of the full cell composed of LFP NP-based electrode as a cathode and Fe_3O_4 NP-based electrode as an anode, and photographical images of TOA-Ag NP and TOA-Cu NP-based electrodes.

AUTHORS' CONTRIBUTIONS

D.N. and M.K. contributed equally to this manuscript. All authors reviewed the final manuscript.

ACKNOWLEDGMENTS

This work was supported by a National Research Foundation of Korea (NRF) grant funded by the Korea government (Grant No. 2019R1A4A1027627).

DATA AVAILABILITY

The data that support the findings of this study are available within the article and its [supplementary material](#).

REFERENCES

- 1 J. Ren, Y. Zhang, W. Bai, X. Chen, Z. Zhang, X. Fang, W. Weng, Y. Wang, and H. Peng, *Angew. Chem.* **126**(30), 7998 (2014).
- 2 S. Liu, Z. Wang, C. Yu, H. B. Wu, G. Wang, Q. Dong, J. Qiu, A. Eychmüller, and X. W. (D.) Lou, *Adv. Mater.* **25**(25), 3462 (2013).
- 3 L. Liu, Y. Yu, C. Yan, K. Li, and Z. Zheng, *Nat. Commun.* **6**, 7260 (2015).
- 4 Y.-H. Lee, J.-S. Kim, J. Noh, I. Lee, H. J. Kim, S. Choi, J. Seo, S. Jeon, T.-S. Kim, J.-Y. Lee, and J. W. Choi, *Nano. Lett.* **13**(11), 5753 (2013).
- 5 H. Lin, W. Weng, J. Ren, L. Qiu, Z. Zhang, P. Chen, X. Chen, J. Deng, Y. Wang, and H. Peng, *Adv. Mater.* **26**(8), 1217 (2014).
- 6 P. Poizot, S. Laruelle, S. Grugeon, L. Dupont, and J.-M. Tarascon, *Nature* **407**, 496 (2000).
- 7 P. Simon and Y. Gogotsi, *Nat. Mater.* **7**, 845 (2008).
- 8 S.-H. Yu, S. H. Lee, D. J. Lee, Y.-E. Sung, and T. Hyeon, *Small* **12**(16), 2146 (2016).
- 9 K. Cao, L. Jiao, H. Liu, Y. Liu, Y. Wang, Z. Guo, and H. Yuan, *Adv. Energy Mater.* **5**(4), 1401421 (2015).
- 10 K. Cao, L. Jiao, Y. Liu, H. Liu, Y. Wang, and H. Yuan, *Adv. Funct. Mater.* **25**(7), 1082 (2015).
- 11 Y. Yang, Z. Peng, G. Wang, G. Ruan, X. Fan, L. Li, H. Fei, R. H. Hauge, and J. M. Tour, *ACS Nano* **8**(7), 7279 (2014).
- 12 L. Hu, F. L. Mantia, H. Wu, X. Xie, J. McDonough, M. Pasta, and Y. Cui, *Adv. Energy Mater.* **1**(6), 1012 (2011).
- 13 J.-S. Kim, Y.-H. Lee, I. Lee, T.-S. Kim, M.-H. Ryou, and J. W. Choi, *J. Mater. Chem. A* **2**(28), 10862 (2014).
- 14 Y. Ko, M. Kwon, W. K. Bae, B. Lee, S. W. Lee, and J. Cho, *Nat. Commun.* **8**, 536 (2017).
- 15 Y. Ko, M. Kwon, Y. Song, S. W. Lee, and J. Cho, *Adv. Funct. Mater.* **28**(46), 1804926 (2018).
- 16 G. F. Yang, K. Y. Song, and S. K. Joo, *J. Mater. Chem. A* **2**(46), 19648 (2014).
- 17 Y.-L. Ding, C. Wu, P. Kopold, P. A. van Aken, J. Maier, and Y. Yu, *Small* **11**(45), 6026 (2015).
- 18 G. Gao, Y. Xiang, S. Lu, B. Dong, S. Chen, L. Shi, Y. Wang, H. Wu, Z. Li, A. Abdelkader, K. Xi, and S. Ding, *Nanoscale* **10**(3), 921 (2018).
- 19 G. X. Pan, F. Cao, Y. J. Zhang, and X. H. Xia, *Mater. Res. Bull.* **98**, 70 (2018).
- 20 R. Zou, Q. Liu, G. He, M. F. Yuen, K. Xu, J. Hu, I. P. Parkin, C.-S. Lee, and W. Zhang, *Adv. Energy Mater.* **7**(2), 1601363 (2017).
- 21 L. Shen, B. Ding, P. Nie, G. Cao, and X. Zhang, *Adv. Energy Mater.* **3**(11), 1484 (2013).
- 22 S. H. Ha, K. H. Shin, H. W. Park, and Y. J. Lee, *Small* **14**(43), 1703418 (2018).
- 23 Y. Zhu, M. Yang, Q. Huang, D. Wang, R. Yu, J. Wang, Z. Zheng, and D. Wang, *Adv. Mater.* **32**(7), 1906205 (2020).
- 24 J.-M. Son, S. Oh, S.-H. Bae, S. Nam, and I.-K. Oh, *Adv. Energy Mater.* **9**(18), 1900477 (2019).
- 25 Y. Guo, M. T. Otle, M. Li, X. Zhang, S. K. Sinha, G. M. Treich, and G. A. Sotzing, *ACS Appl. Mater. Interfaces* **8**(40), 26998 (2016).
- 26 L. Hu, J. W. Choi, Y. Yang, S. Jeong, F. L. Mantia, L.-F. Cui, and Y. Cui, *Proc. Natl. Acad. Sci. U. S. A.* **106**(51), 21490 (2009).
- 27 N. Kurra, B. Ahmed, Y. Gogotsi, and H. N. Alshareef, *Adv. Energy Mater.* **6**(24), 1601372 (2016).
- 28 P. Chen, H. Chen, J. Qiu, and C. Zhou, *Nano Res.* **3**, 594 (2010).
- 29 H. M. Lee, S.-Y. Choi, A. Jung, and S. H. Ko, *Angew. Chem.* **125**(30), 7872 (2013).
- 30 Q. Zhang, J. Wang, J. Dong, F. Ding, X. Li, B. Zhang, S. Yang, and K. Zhang, *Nano Energy* **13**, 77 (2015).
- 31 S. Luo, K. Wang, J. Wang, K. Jiang, Q. Li, and S. Fan, *Adv. Mater.* **24**(17), 2294 (2012).
- 32 T. Gu, Z. Cao, and B. Wei, *Adv. Energy Mater.* **7**(18), 1700369 (2017).
- 33 R. Mo, S. O. Tung, Z. Lei, G. Zhao, K. Sun, and N. A. Kotov, *ACS Nano* **9**(5), 5009 (2015).
- 34 O. Toprakci, L. Ji, Z. Lin, H. A. K. Toprakci, and X. Zhang, *J. Power Sources* **196**(18), 7692 (2011).
- 35 Z. Wang, H. Wang, S. Ji, H. Wang, D. J. L. Brett, and R. Wang, *J. Alloys Compd.* **814**, 151789 (2020).
- 36 T. Xia, X. Zhang, J. Zhao, Q. Li, C. Ao, R. Hu, Z. Zheng, W. Zhang, C. Lu, and Y. Deng, *ACS Sustainable Chem. Eng.* **7**(5), 5231 (2019).
- 37 M. F. De Riccardis, D. Carbone, V. Martina, M. Re, B. Bozzini, and L. D'Urzo, *Appl. Surf. Sci.* **255**(7), 4309 (2009).
- 38 K. Chen, R. Pathak, A. Gurung, K. M. Reza, N. Ghimire, J. Pokharel, A. Baniya, W. He, J. J. Wu, Q. (Q.) Qiao, and Y. Zhou, *J. Mater. Chem. A* **8**(4), 1911 (2020).
- 39 G. Decher, *Science* **277**(5330), 1232 (1997).
- 40 S. S. Shiratori and M. F. Rubner, *Macromolecules* **33**(11), 4213 (2000).
- 41 S. W. Lee, N. Yabuuchi, B. M. Gallant, S. Chen, B. S. Kim, P. T. Hammond, and Y. Shao-Horn, *Nat. Nanotechnol.* **5**, 531 (2010).
- 42 Y. Kim, J. Zhu, B. Yeom, M. D. Prima, X. Su, J. Kim, S. J. Yoo, C. Uher, and N. A. Kotov, *Nature* **500**, 59 (2013).
- 43 S. Y. Kim, J. Hong, R. Kaviani, S. W. Lee, M. N. Hyder, Y. Shao-Horn, and T. Hammond, *Energy Environ. Sci.* **6**(3), 888 (2013).
- 44 S. Kang, D. Nam, J. Choi, J. Ko, D. Kim, C. H. Kwon, J. Huh, and J. Cho, *ACS Appl. Mater. Interfaces* **11**(12), 12032 (2019).

- ⁴⁵S. W. Lee, B. M. Gallant, H. R. Byon, P. T. Hammond, and Y. Shao-Horn, *Energy Environ. Sci.* **4**(6), 1972 (2011).
- ⁴⁶M. N. Hyder, S. W. Lee, F. C. Cebeci, D. J. Schmidt, Y. Shao-Horn, and P. T. Hammond, *ACS Nano* **5**(11), 8552 (2011).
- ⁴⁷Y. Zhang, C. J. Sheehan, J. Zhai, G. Zou, H. Luo, J. Xiong, Y. T. Zhu, and Q. X. Jia, *Adv. Mater.* **22**(28), 3027 (2010).
- ⁴⁸A. Zabet-Khosousi and A.-A. Dhirani, *Chem. Rev.* **108**(10), 4072 (2008).
- ⁴⁹J. Jiang, W. Liu, J. Chen, and Y. Hou, *ACS Appl. Mater. Interfaces* **4**(6), 3062 (2012).
- ⁵⁰P. Martinez, F. Ruiz, J. Curiale, M. Vasquez Mansilla, R. D. Zysler, L. Dada, M. S. Moreno, L. Rodríguez, D. Fregenal, G. Bernardi, and E. Lima, Jr., *J. Phys. D: Appl. Phys.* **49**(33), 335302 (2016).
- ⁵¹O. Xiuqin, P. Lin, G. Haichen, W. Yichen, and L. Jianwei, *J. Mater. Chem.* **22**(18), 9064 (2012).
- ⁵²F. Fathollahi, M. Javanbakht, H. Omidvar, and M. Ghaemi, *J. Alloys. Compd.* **627**, 146 (2015).
- ⁵³J. Choi, D. Nam, D. Shin, Y. Song, C. H. Kwon, I. Cho, S. W. Lee, and J. Cho, *ACS Nano* **13**(11), 12719 (2019).
- ⁵⁴J. Wang, Y. Zhang, M. Yi, Z. Shen, L. Liu, H. Liu, and X. Zhang, *Energy Technol.* **7**(3), 1800634 (2019).
- ⁵⁵S. Lee, Y. Song, Y. Ko, Y. Ko, J. Ko, C. H. Kwon, J. Huh, S.-W. Kim, B. Yeom, and J. Cho, *Adv. Mater.* **32**(7), 1906460 (2020).
- ⁵⁶H. Gao, Q. Wu, Y. Hu, J. P. Zheng, K. Amine, and Z. Chen, *J. Phys. Chem. Lett.* **9**(17), 5100 (2018).
- ⁵⁷C. H. Kwon, Y. Ko, D. Shin, M. Kwon, J. Park, W. K. Bae, S. W. Lee, and J. Cho, *Nat. Commun.* **9**, 4479 (2018).
- ⁵⁸S. Zhao, Y. Li, H. Yin, Z. Liu, E. Luan, F. Zhao, Z. Tang, and S. Liu, *Sci. Adv.* **1**(10), e1500372 (2015).
- ⁵⁹M. Brust, M. Walker, D. Bethell, D. J. Schiffrin, and R. Whyman, *J. Chem. Soc., Chem. Commun.* **7**, 801 (1994).
- ⁶⁰J. Fink, C. J. Kiely, D. Bethell, and D. J. Schiffrin, *Chem. Mater.* **10**(3), 922 (1998).
- ⁶¹M. Kanehara, H. Koike, T. Yoshinaga, and T. Teranishi, *J. Am. Chem. Soc.* **131**(49), 17736 (2009).
- ⁶²S. Sun, H. Zeng, D. B. Robinson, S. Raoux, P. M. Rice, S. X. Wang, and G. Li, *J. Am. Chem. Soc.* **126**(1), 273 (2004).
- ⁶³K. Nielsch, F. Müller, A. Li, and U. Gösele, *Adv. Mater.* **12**(8), 582 (2000).
- ⁶⁴H. Alimadadi, A. B. Fanta, T. Kasama, M. A. J. Somers, and K. Pantleon, *Surf. Coat. Technol.* **299**, 1 (2016).
- ⁶⁵J. P. Hoare, *J. Electrochem. Soc.* **133**(12), 2491 (1986).
- ⁶⁶M. S. A. Farisi, S. Hertel, M. Wiemer, and T. Otto, *Micromachines* **9**(11), 589 (2018).
- ⁶⁷X. Tu, J. Zhang, M. Zhang, Y. Cai, H. Lang, G. Tian, and Y. Wang, *RSC Adv.* **7**(24), 14790 (2017).
- ⁶⁸A. P. Abbott, F. Qiu, H. M. A. Abood, M. R. Ali, and K. S. Ryder, *Phys. Chem. Chem. Phys.* **12**(8), 1862 (2010).
- ⁶⁹D. A. Buttry, *Advanced in Electroanalytical Chemistry: Applications of the QCM to Electrochemistry* (Marcel Dekker Inc., New York, 1991).